

Final Technical Report for FA9550-09-C-0207

**“Partitioning of Electromagnetic Energy
Inputs to the Thermosphere during
Geomagnetic Disturbances”**

June 2012

Prepared by:

**Keith Siebert, Principal Investigator
Applied Research Associates (ARA)
39 Simon Street, #15
Nashua, NH 03060**

Prepared for:



REPORT DOCUMENTATION PAGE				Form Approved OMB No. 0704-0188	
Public reporting burden for this collection of information is estimated to average 1 hour per response, including the time for reviewing instructions, searching existing data sources, gathering and maintaining the data needed, and completing and reviewing this collection of information. Send comments regarding this burden estimate or any other aspect of this collection of information, including suggestions for reducing this burden to Department of Defense, Washington Headquarters Services, Directorate for Information Operations and Reports (0704-0188), 1215 Jefferson Davis Highway, Suite 1204, Arlington, VA 22202-4302. Respondents should be aware that notwithstanding any other provision of law, no person shall be subject to any penalty for failing to comply with a collection of information if it does not display a currently valid OMB control number. PLEASE DO NOT RETURN YOUR FORM TO THE ABOVE ADDRESS.					
1. REPORT DATE (DD-MM-YYYY) 30-06-2012		2. REPORT TYPE Final		3. DATES COVERED (From - To) 30-09-2009 - 30-06-2012	
4. TITLE AND SUBTITLE Final Technical Report for FA9550-09-C-0207 Partitioning of electromagnetic energy inputs into the thermosphere during geomagnetic disturbances				5a. CONTRACT NUMBER FA9550-09-C-0207	
				5b. GRANT NUMBER	
				5c. PROGRAM ELEMENT NUMBER	
6. AUTHOR(S) Siebert, Keith D				5d. PROJECT NUMBER	
				5e. TASK NUMBER	
				5f. WORK UNIT NUMBER	
7. PERFORMING ORGANIZATION NAME(S) AND ADDRESS(ES) Applied Research Associates 39 Simon Street, #15 Nashua, NH 03060				8. PERFORMING ORGANIZATION REPORT NUMBER	
9. SPONSORING / MONITORING AGENCY NAME(S) AND ADDRESS(ES) AFOSR/NE (Dr. Kent Miller) 875 North Randolph Street Suite 325, Room 3112 Arlington, VA 22203				10. SPONSOR/MONITOR'S ACRONYM(S)	
				11. SPONSOR/MONITOR'S REPORT NUMBER(S) AFRL-OSR-VA-TR-2012-1160	
12. DISTRIBUTION / AVAILABILITY STATEMENT DISTRIBUTION A: APPROVED FOR PUBLIC RELEASE					
13. SUPPLEMENTARY NOTES					
14. ABSTRACT We investigate a number of fundamental processes that govern thermospheric response to electromagnetic energy inputs. Using a sophisticated numerical model of the coupled solar wind - magnetosphere - ionosphere - thermosphere, we focus on three main subject areas: Poynting flux energy partitioning, horizontal neutral density structures, and feedback of neutral dynamics to the coupled system. Simulations show that approximately 90 per cent of the Poynting flux into the thermosphere goes into Joule heating under steady state conditions. Under southward IMF orientations, local height-integrated Joule heating rates overestimate Poynting flux in regions of high conductance, and underestimate Poynting flux in regions of lower conductance, confirming the prediction of Richmond (2010). At E-region altitudes, neutral density cell structure is correlated with divergences of the J X B force. These divergences arise because of Hall conductivity effects which rotate current-density and ion-velocity vectors from their non-divergent F-region patterns.					
15. SUBJECT TERMS					
16. SECURITY CLASSIFICATION OF:			17. LIMITATION OF ABSTRACT SAR	18. NUMBER OF PAGES 19	19a. NAME OF RESPONSIBLE PERSON Keith D. Siebert
a. REPORT	b. ABSTRACT	c. THIS PAGE			19b. TELEPHONE NUMBER (include area code) (603) 595-2139

Table of Contents

1. Summary	1
2. Introduction	1
2.1. Poynting Flux Energy Partitioning	1
2.2. Investigation Objectives	3
2.3. Organization of Report	4
3. Methods, Assumptions and Procedures	4
3.1. Integrated Space Weather Prediction Model	4
3.2. Simulation Methods	4
4. Results and Discussion	6
4.1. Dependence of Energy Partitioning on IMF Clock Angle and Season	6
4.2. Effect of Drag-Driven Neutral Winds on Thermospheric Density	10
4.3. Feedback Mechanisms	15
5. Conclusions	16
6. Personnel Supported	17
7. Publications	18
8. Interactions / Transitions	18
9. References.....	18

List of Figures

Figure 1. Pedersen and Hall conductance maps for (a) vertical geographic pole (northern hemisphere); (b) solsticial pole (northern hemisphere); (c) solsticial pole (southern hemisphere, viewed through the northern hemisphere).....	6
Figure 2. Joule dissipation rate (left) and mechanical work rate (right) at 120 km altitude, northern polar region, IMF South. Red star in left plot indicates intersection point of radial line used for 1-D plot in Figure 3.	7
Figure 3. Joule heating rate as a function of altitude in units of energy density per time (top) and specific energy per time (bottom).....	8

Figure 4. Poynting flux maps (left) and height-integrated power maps (right) in northern polar region for (a) South IMF; (b) East IMF; (c) North IMF. On each map the “+” symbol locates peak value.	9
Figure 5. Ion velocity vectors at 400 km (left) and 120 km (right) for (a) IMF South; (b) IMF East; (c) IMF North. Vectors are color-coded according to magnitude with black indicating speeds equal or greater than 1 km/s for (a) and (b), and 0.5 km/s for (c).....	11
Figure 6. Neutral velocity vectors in the rotational frame (top) and neutral density contours (bottom) at 400 km. From left to right: IMF East – northern hemisphere; IMF East – southern hemisphere; IMF South; IMF North. Vectors are color-coded according to magnitude with black indicating speeds equal or greater than 1 km/s.	12
Figure 7. Figure 6 from Kwak et al. (2009). Difference densities at 400 km altitude over the southern hemisphere for different IMF orientations.	13
Figure 8. Neutral velocity vectors in the rotational frame at 120 km. From left to right: IMF East – northern hemisphere; IMF East – southern hemisphere; IMF South; IMF North. Vectors are color-coded according to magnitude with black indicating speeds equal or greater than 0.1 km/s.....	14
Figure 9. $\mathbf{J} \times \mathbf{B}$ vectors (top) and neutral density contours (bottom) at 120 km. From left to right: IMF East – northern hemisphere; IMF East – southern hemisphere; IMF South; IMF North. Vectors are color-coded according to magnitude with black indicating $\mathbf{J} \times \mathbf{B}$ force magnitudes equal or greater than 1×10^{-11} dyne/cm ³	14
Figure 10. Electrodynamical quantities for simulations with zero neutral velocity (left column) and steady-state neutral velocity (right column). (a) $\mathbf{J} \times \mathbf{B}$ vectors at 300 km altitude; (b) Parallel current density contours at 500 km altitude (orange-red indicates current into ionosphere; blue indicates current out of the ionosphere); (c) $\mathbf{J} \times \mathbf{B}$ vectors at 120 km altitude	17

List of Tables

Table 1. Simulation Parameters	5
Table 2. Electromagnetic Power Energy Partitioning	8

1. Summary

We investigate a number of fundamental processes that govern thermospheric response to electromagnetic energy inputs. Using a sophisticated numerical model of the coupled solar wind – magnetosphere – ionosphere – thermosphere, we focus on three main subject areas: Poynting flux energy partitioning, horizontal neutral density structures, and feedback of neutral dynamics to the coupled system.

Numerical simulations show that approximately 90 per cent of the Poynting flux into the thermosphere goes into Joule heating under steady-state conditions. Thus in a global sense, measurements of Joule heating rates provide a good approximation to total electromagnetic energy input; however, locally this is not always the case. Under southward IMF orientations, local height-integrated Joule heating rates overestimate Poynting flux in regions of high conductance, and underestimate Poynting flux in regions of lower conductance. This confirms the prediction of Richmond (2010).

We confirmed the analysis of Schoendorf et al (1996) that attributed the existence of anti-cyclonic low density cells to centrifugal effects in the presence of large drag-driven neutral flows. At E-region altitudes, we present a new theory that relates neutral density cell structure to divergences of the $\vec{J} \times \vec{B}$ force. At E-region altitudes these divergences arise because of Hall conductivity effects which rotate current-density and ion-velocity vectors from their non-divergent F-region patterns.

We find that increases in neutral wind speeds under steady driving conditions do not significantly alter electromagnetic energy flows into the ionosphere / thermosphere. While F-region closure currents are significantly reduced, the much larger E-region closure currents are not, owing to the much larger neutral densities, and thus much greater coupling times. Thus parallel current densities and Poynting fluxes into the ionosphere / thermosphere are not greatly altered by neutral dynamics.

2. Introduction

The dynamics of Earth's thermosphere represents a key challenge in the area of SSA. Aerodynamic drag is the largest source of uncertainty in precision orbit determination for satellites operating below about 600 km altitude. Aerospace missions affected by drag errors include satellite orbit location and prediction, collision avoidance warnings, reentry prediction, lifetime estimates, and attitude dynamics (Marcos, 2006). Because aerodynamic drag is dependent on thermospheric density, nowcasting and forecasting of the state of the thermosphere is necessary for reduction of drag errors.

2.1. Poynting Flux Energy Partitioning

The thermosphere is one element of a complex coupled system that includes the ionosphere, magnetosphere and the sun. Thermospheric density responds to energy inputs generated within this system. The sun is the ultimate driver, and provides energy in the form of EUV radiation and solar wind kinetic energy. Solar EUV radiation directly heats and ionizes the thermosphere. Solar wind energy is transferred indirectly through an interaction with Earth's magnetic field that gives rise to an electromagnetic dynamo. Dynamo energy flowing into the thermosphere is mediated by the ionosphere. Unlike solar EUV radiation to which the thermosphere responds passively (i.e. without feedback), the thermosphere is a reactive element in the coupled system through which solar wind energy flows. Thus the thermospheric response can alter energy flow through the system. It is this aspect of thermospheric dynamics that presents the greatest challenge to modeling efforts because it

requires a treatment of the solar wind – magnetosphere – ionosphere – thermosphere system in its entirety.

The two primary sources for energy transfer from the solar wind dynamo to the thermosphere are particle precipitation and electromagnetic field energy or Poynting flux. This report focuses on the response of the thermosphere to Poynting flux. While particle precipitation does produce heating of the thermosphere, in general the total power input from Poynting flux is greater than that of particle precipitation by roughly a factor of two (Waters, 2004). In our study, particle precipitation is investigated primarily for its role in altering ionospheric conductance profiles. Variations in ionospheric conductance alter the total power delivered to the thermosphere by Poynting flux.

The mechanism by which Poynting flux is transferred to the thermosphere is most easily understood by considering the thermosphere and ionosphere to be separate hydrodynamic and magnetohydrodynamic (MHD) fluids respectively. Convection of the ionosphere fluid associated with the Poynting flux electric field exerts a drag force on the thermosphere fluid to which it is collisionally coupled. This accelerates the thermosphere and heats it frictionally. In addition to momentum transfer, collisional processes transfer heat between the ion and neutral fluids.

Polar Poynting flux distributions depend on IMF orientation. Using DE2 data, Gary et al. (1995) showed that for southward IMF Poynting flux was greatest in the auroral zones at dawn and dusk. For northward IMF, they found that the Poynting flux was greatest in the polar cap near noon. Waters et al. (2004) also showed Poynting flux peaking in the auroral zones for southward IMF, but noted that the Poynting flux was not uniform in local time and tended to maximize in “hot spots” whose location and extent differs between hemispheres and depends on the IMF. They also found that the total Poynting flux power integrated over the polar cap is an appreciable fraction of the total electromagnetic energy, accounting for up to half as much as the auroral zone input.

The paradigm for partitioning Poynting-flux energy into thermal and mechanical energy pools is based on Poynting’s theorem, which for time-independent fields can be written as (e.g. Thayer, 1995):

$$-\vec{\nabla} \cdot \vec{S} = -\vec{\nabla} \cdot \vec{E} \times \delta \vec{B} = \vec{J} \cdot \vec{E} = \vec{J} \cdot \vec{E}' + \vec{U} \cdot \vec{J} \times \vec{B}$$

Here \vec{S} is the Poynting flux, $\delta \vec{B}$ is the perturbation magnetic field (deviation from Earth’s background dipole field), \vec{J} is the electric current density, \vec{E} the electric field in the inertial frame, \vec{E}' is the electric in the frame of the moving neutral fluid, and \vec{U} is the neutral fluid velocity. The $\vec{J} \cdot \vec{E}'$ term on the far right hand side is typically identified as Joule dissipation that goes directly into thermal energy. However, care must be taken with this interpretation. Vasyliunas and Song (2005) argue that “Joule dissipation” is a misnomer and this heating term is more accurately described as frictional heating arising from the relative motion of plasma and neutral fluids. This heating causes the thermosphere to expand upward and thus produces density enhancements along satellite orbit tracks.

The $\vec{U} \cdot \vec{J} \times \vec{B}$ term represents the portion of the electromagnetic energy that goes into mechanical work done on the neutral wind. When the ionosphere is near equilibrium a force balance exists between the neutral-ion drag force (i.e. the drag force exerted by the neutrals on the ions) and the $\vec{J} \times \vec{B}$ force:

$$\rho_i v_{in} (\vec{v}_i - \vec{v}_n) = \vec{J} \times \vec{B}$$

Here ρ_i is the ion mass density, v_{in} is the ion-neutral collision frequency, and \vec{v}_i and \vec{v}_n are the ion and neutral velocities respectively. By momentum conservation, the ion-neutral drag force is exactly equal to the neutral-ion drag force (i.e. the drag force exerted by the ions on the neutrals). In this way the $\vec{J} \times \vec{B}$ force is directly transferred to the neutrals. The mechanical work term can thus be viewed as the work done by the $\vec{J} \times \vec{B}$ force on the neutrals. Unlike the Joule heating term, the mechanical work term

can be positive or negative. Positive work indicates energy transfer from ions to neutrals; negative work indicates energy transfer from neutrals to ions.

The presence of the neutral wind adds significant complexity to the energy partitioning problem, and is the reason it has become a subject of detailed study (Thayer et al., 1995, 1998, 2000). These studies have shown that ignoring it can result in significant errors in the determination of global thermospheric heating rates. Furthermore, for given solar wind conditions, electromagnetic energy partitioning depends on spatial location. Over the polar cap Poynting flux is more heavily weighted toward the mechanical energy pool, while auroral-zone Poynting flux is weighted toward thermal (Waters et al., 2004).

Like Joule dissipation, electromagnetic energy that goes into the mechanical energy of neutral winds can also alter thermospheric density profiles. The ultimate response of the thermosphere is governed by the interplay of the drag force with other neutral forces such as pressure gradients, centrifugal and Coriolis forces, and viscosity. Illustrating this point, Schoendorf et al. (1996) describe a mechanism by which the neutral winds drive the high-latitude density structure.

The mechanism is initiated by ion drag forcing high-latitude neutral winds into a cellular circulation pattern similar to the ion velocity pattern. They find that for slower neutral circulation speeds, the thermosphere behaves as expected for typical geostrophic flow: pressure gradient and Coriolis forces oppose each other. Therefore, in the dusk sector where flow is typically anticyclonic, neutral circulation encompasses a high density region while in the dawn sector where flow is typically cyclonic, neutral circulation encompasses a low density region. When situations occur in which ion drag causes neutral velocities to be large, thermospheric density behavior on the dawn side remains the same, but in the anticyclonic dusk sector density is depleted instead of enhanced. The mechanism for this depletion was posited to be an anomalous “antibaric” low for which the pressure gradient and Coriolis forces act in the same direction, towards the center of the circulation cell. Schoendorf et al. also determined that high latitude Joule heating is responsible for the general increase in neutral densities as geomagnetic conditions strengthen, while the aforementioned neutral circulation reduces densities around circulation centers. The combination of these influences produces the structure seen in high-latitude neutral mass densities. Using CHAMP data, Kwak et al. (2009) came to a similar conclusion when they investigated high-latitude neutral densities for various IMF conditions, and determined that ionospheric convection drives the thermospheric winds which influence the high latitude neutral densities, and also that auroral and cusp region density variations are influenced by local heating associated with ionospheric currents.

The thermosphere is an active element of the coupled system. Electromagnetic energy input into the thermosphere changes properties of the thermosphere that alter subsequent energy partitioning, and can alter the Poynting flux itself as the global electric circuit reconfigures to accommodate changes to its fundamental elements. Such changes are generally on longer time scales, and are complicated by the different response times of electric field, conductivity, and neutral wind. Determination of the operative feedback loops within the coupled system is critical for understanding its evolution and for developing accurate predictive models.

2.2. Investigation Objectives

Our investigation was organized by four different topic areas:

- 1) Magnetic field effects: How does IMF orientation and dipole tilt affect electromagnetic energy input and partitioning into the thermosphere?

- 2) Ion drag effects: How does the rotation of the ion velocity pattern with altitude (due to Hall conductivity) affect neutral density distributions?
- 3) Feedback mechanisms: How do thermospheric dynamics alter electromagnetic energy input and partitioning?

2.3. Organization of Report

Section 3 contains a brief description of the simulation model, and the input parameters that specified the set of simulations we performed for this investigation. We also describe diagnostics we used to analyze simulation data sets. Section 4 is divided into three sections, with each section devoted to one of the topic areas discussed above. Section 5 contains the main conclusions from this investigation.

3. Methods, Assumptions and Procedures

3.1. Integrated Space Weather Prediction Model

The simulation tool used in this investigation was the Integrated Space Weather Prediction Model (ISM). ISM is a global model of the coupled ionosphere – thermosphere – magnetosphere system. It has been developed under sponsorship of the Defense Threat Reduction Agency (DTRA) by a technical team that comprises industry (SPARTA and ARA) and academia (Boston University, Dartmouth College, and Rice University). AFRL has also participated during ISM development in an advisory capacity. ISM has been used in a variety of scientific investigations sponsored by NASA and NSF.

ISM is based on the equations of Two-Fluid MHD (White, et al., 2001). The two fluids are a plasma fluid (representing the ion-electron plasma of the ionosphere, magnetosphere, and solar wind) and a neutral fluid (representing the atomic and molecular species of the thermosphere). The plasma and neutral fluids are coupled collisionally (momentum and energy exchange) and chemically. In regions where the neutral density goes to zero, Two-Fluid MHD reduces to the standard MHD equations.

ISM advances the Two-Fluid MHD equations on a grid system that extends continuously from the “bottom” of the ionosphere (typically set at 80 km) upward through the magnetosphere and into the solar wind. The outer grid boundaries are typically set at 30 R_E sunward, 300 R_E tailward, and 50 R_E dawn and duskward. Since the MHD equations are essentially statements of the conservation of mass, momentum and energy, ISM’s use of a computational grid that continuously spans the relevant physical volume, combined with a numerical scheme that preserves the conservation properties of the equations, makes it well-suited for studying energy flow within the solar wind – magnetosphere – ionosphere – thermosphere system.

Conductivities are not explicitly computed in ISM except as outputs for diagnostic purposes. Rather, the ion-neutral coupling is expressed in terms of collision frequencies (momentum coupling) and heat-transfer coefficients (energy coupling). The approach is consistent with the formulation of Vasyliunas and Song (2005) and permits expression of Joule heating in terms of the frictional heating term, $\rho_i v_{in} |\vec{v}_i - \vec{v}_n|^2$.

3.2. Simulation Methods

Parametric Variations

Table 1 lists parametric variations performed for this study. All simulations had a common solar wind velocity and density of 400 km/s and 5 cm⁻³ respectively. A rotating Earth was used with the geomagnetic and geographic poles aligned. Simulations were performed in three phases. First a quasi-

Partitioning of Electromagnetic Energy Inputs to the Thermosphere
Final Report for FA9550-09-C-0207

steady magnetosphere was modeled with a static thermosphere to establish the ionospheric driver. This driver was then used to “spin-up” the thermosphere for a simulation time interval of 24 hours, after which the thermosphere was also quasi-steady. Thereafter simulations were fully coupled with fully-dynamic magnetosphere, ionosphere, and thermosphere regions.

Table 1. Simulation Parameters

Case	IMF B_x (nT)	IMF B_y (nT)	IMF B_z (nT)	Conductance	Orientation of Geographic Pole
Moderate Driver	0.	0.	-2.	Uniform ($\Sigma_P = \Sigma_H = 1$ mho)	Vertical
IMF South	0.	0.	-5.	Solar + Auroral	Vertical
IMF East	0.	5.	0.	Solar + Auroral	Vertical
IMF North	0.	0.	5.	Solar + Auroral	Vertical
Summer Solstice	0.	0.	-5.	Solar + Auroral	Northern Hemisphere Summer Solstice
Strong Driver	0.	0.	-20.	Solar + Auroral	Vertical
IMF Rotation	0.	0.	-5. To +5.	Solar + Auroral	Vertical

Figure 1 shows Hall and Pedersen conductance profiles for the cases labeled “Solar + Auroral” in the conductance column of Table 1. These conductance profiles are not specified directly; rather, conductances are determined by specification of solar and auroral ionization sources. Figure 1 contains separate plots for northern and southern hemispheres for the “Summer Solstice” case, since conductances are not symmetric for that case.

Diagnostics

We used the ISM_VIEW visualization application to generate contour plots and vector streamline plots of both native ISM cell quantities as well as derived quantities such as Poynting flux. Because ISM carries the perturbation magnetic field, $\overline{\delta B}$, as a cell quantity throughout its computational volume, we are able to generate maps of the Poynting flux, $\vec{E} \times \overline{\delta B}$, on altitude surfaces at the top of the thermosphere. We used separate modules to integrate the Poynting flux over this surface to compute the total electromagnetic energy input into the thermosphere. We also created modules to compute the volume integrals of the Joule heating rate and the mechanical work rate. With these diagnostics we were able to compute both the total energy input and energy partitioning for all of the cases listed in Table 1.

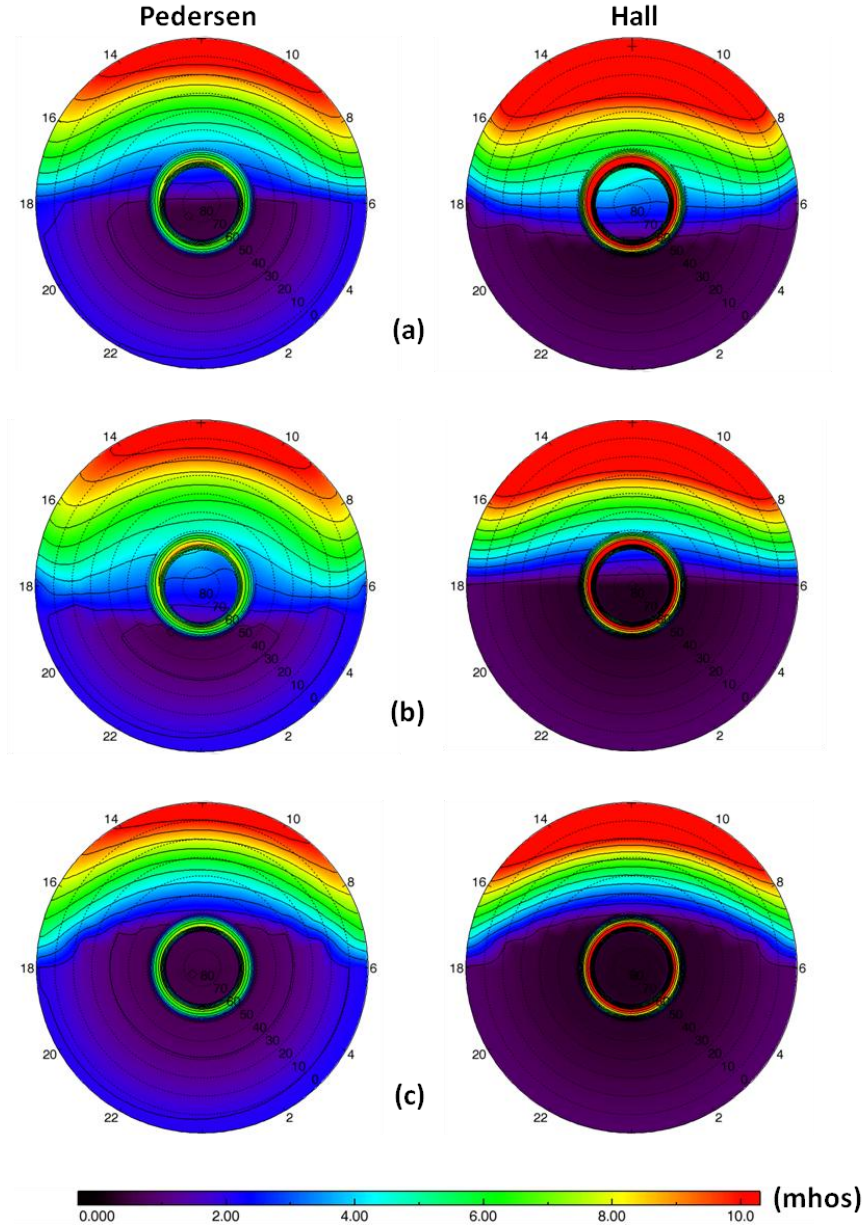


Figure 1. Pedersen and Hall conductance maps for (a) vertical geographic pole (northern hemisphere); (b) solstitial pole (northern hemisphere); (c) solstitial pole (southern hemisphere, viewed through the northern hemisphere)

4. Results and Discussion

4.1. Dependence of Energy Partitioning on IMF Clock Angle and Season

In this section we look at the spatial distribution of Poynting flux, Joule dissipation, and mechanical work rate, as well as height, area, and volume integrals of these quantities over the poles. One of the goals of this section is to assess the degree to which Joule dissipation rates can be used in data analyses and model analyses as a surrogate for Poynting flux. Figure 2 contains north-pole contour plots of the Joule dissipation rate and mechanical work rate at 120 km altitude for the IMF South case. Note that

mechanical work rate magnitudes are significantly smaller than Joule dissipation magnitudes. (The color scale for the mechanical work rate plot is a factor of 10 smaller than the scale for the Joule dissipation plot.) Both quantities are peaked in auroral conductance regions, with lesser maxima in the convection throat region. Joule dissipation is a positive definite quantity, while mechanical work rate is a signed quantity. In the mechanical work rate plot, tan colors indicate positive values and blue indicates negative values. The convection throat region is a region of negative mechanical work rate, indicating that neutrals are doing work on the ions in this region; however, the magnitude of this work rate is about a factor of 40 smaller than the Joule dissipation rate.

Figure 3 shows the altitude distribution of the Joule heating rate along a radial line through the red star superimposed on the left plot of Figure 2. The top panel is the volumetric Joule heating rate in units of $\text{erg}/\text{cm}^3\text{-s}$. It exhibits a single peak at approximately 120 km altitude (the altitude of the contour plots in Figure 2). This is not surprising since 120 km is an E-region altitude where conductivities are peaked, and Joule heating goes like $\sigma|E'|^2$, where σ is the conductivity and E' is the electric in the frame of the moving neutrals. The bottom panel of Figure 3 is the specific Joule heating rate in units of $\text{erg}/\text{g-s}$. It corresponds to the time rate of change of neutral temperature, and exhibits both an E-region peak and a much larger F-region peak. The F-region is a local maximum of Pedersen conductance, and although conductance is smaller than in the E-region, the lower neutral density there results in a larger specific heating rate.

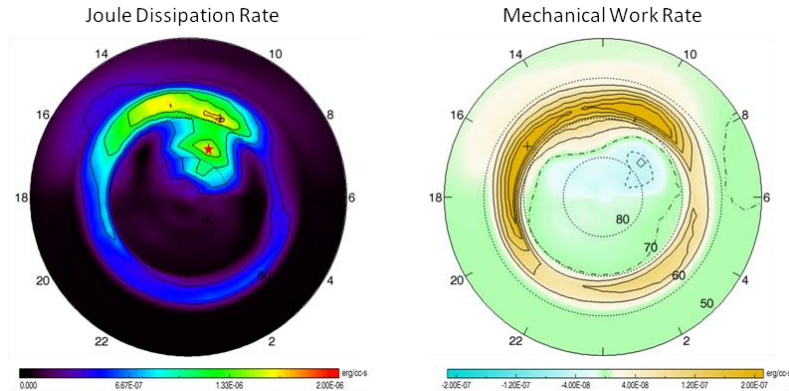


Figure 2. Joule dissipation rate (left) and mechanical work rate (right) at 120 km altitude, northern polar region, IMF South. Red star in left plot indicates intersection point of radial line used for 1-D plot in Figure 3.

From Poynting's theorem we know that in steady-state the volume integral of the sum of Joule heating and mechanical work rates should be equal to the surface integral of Poynting flux normal to an altitude surface above the thermosphere. This assumes that we choose a volume whose latitudinal extent away from the pole is great enough that horizontal Poynting flux is zero at the latitudinal boundary. It also assumes that vertical Poynting flux is zero at the volume's low-altitude boundary. Because our simulations allow us to compute Poynting flux independently from Joule heating and mechanical work rates, we can assess the degree to which they satisfy Poynting's theorem. Table 2 contains the relevant integrated quantities for the IMF South, East, and North simulations. The second column is the Poynting flux integrated over a 500 km altitude surface. The values in this column indicate that the total electromagnetic energy input into the thermosphere decreases as the IMF is rotated from south to north. This is consistent with the findings of other studies (e.g. Weimer, 2004). The third and fourth

columns are the volume integrals of Joule heating and mechanical work rates respectively. The fifth column is the sum of columns three and four. This number should be approximately equal to the integrated Poynting flux in column two. The fractional difference between it and integrated Poynting flux is given in column six. The small values here confirm simulation operation. Exact agreement is not expected given that the simulation is not in an exact steady state.

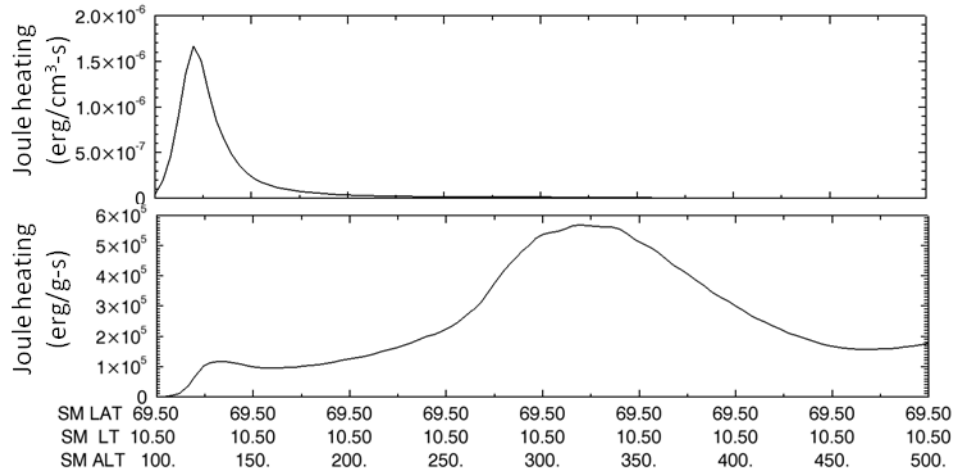


Figure 3. Joule heating rate as a function of altitude in units of energy density per time (top) and specific energy per time (bottom).

Given that simulation results agree with expectations from Poynting's theorem, we can now assess the energy partitioning of Poynting flux into thermal and mechanical energy pools. Column 7 of Table 2 contains the fraction of Poynting flux going into mechanical work. For all IMF orientations shown, mechanical work is on the order of 10 per cent of the total electromagnetic energy going into the thermosphere. This relatively small value indicates that at least in an integrated sense, Joule heating rates account for almost all of the electromagnetic energy input into the ionosphere / thermosphere.

Table 2. Electromagnetic Power Energy Partitioning

Case	Poynting Power (GW)	Joule Heating (GW)	Mechanical Work (GW)	Joule + Mechanical (GW)	Fractional Difference	Mechanical Work Fraction
IMF South	67	57	7.8	65	3%	12%
IMF East	34	28	4.3	32	4%	13%
IMF North	3.7	3.3	0.3	3.6	3%	8%

Next we want to examine whether Joule heating rates correspond to electromagnetic energy input in a local sense. To do this we need to compare Poynting flux maps generated on an altitude surface above the thermosphere with maps of field-line integrated Joule heating rates. The degree to which they agree represents the degree to which Poynting flux at a particular point above the thermosphere is dissipated locally in the flux tube volume below that point, and thus the degree to which field-line integrated Joule

Partitioning of Electromagnetic Energy Inputs to the Thermosphere **Final Report for FA9550-09-C-0207**

heating can approximate local Poynting flux and vice versa. Work by Richmond (2010) showed that this equality can only be satisfied if the side boundary of a local flux tube volume is an equipotential. Figure 4 contains maps of Poynting flux normal to a 500 km altitude surface and maps of height-integrated Joule heating rate for the IMF South, East, and North cases. We have chosen height-integration rather than field-line integration for computational simplicity. For the polar regions under consideration, where field lines are nearly vertical, this should be a good approximation. The color scale for these plots has both negative and positive values since we are plotting a single Poynting flux component (the component normal to the constant-altitude plotting surface), and it is a signed quantity. The convention we use is positive values (tan) indicate flux into the thermosphere, and negative values (blue) indicate flux out of the thermosphere. Figure 4 shows that for all of these steady-state cases, essentially all of the Poynting flux is directed downward into the thermosphere.

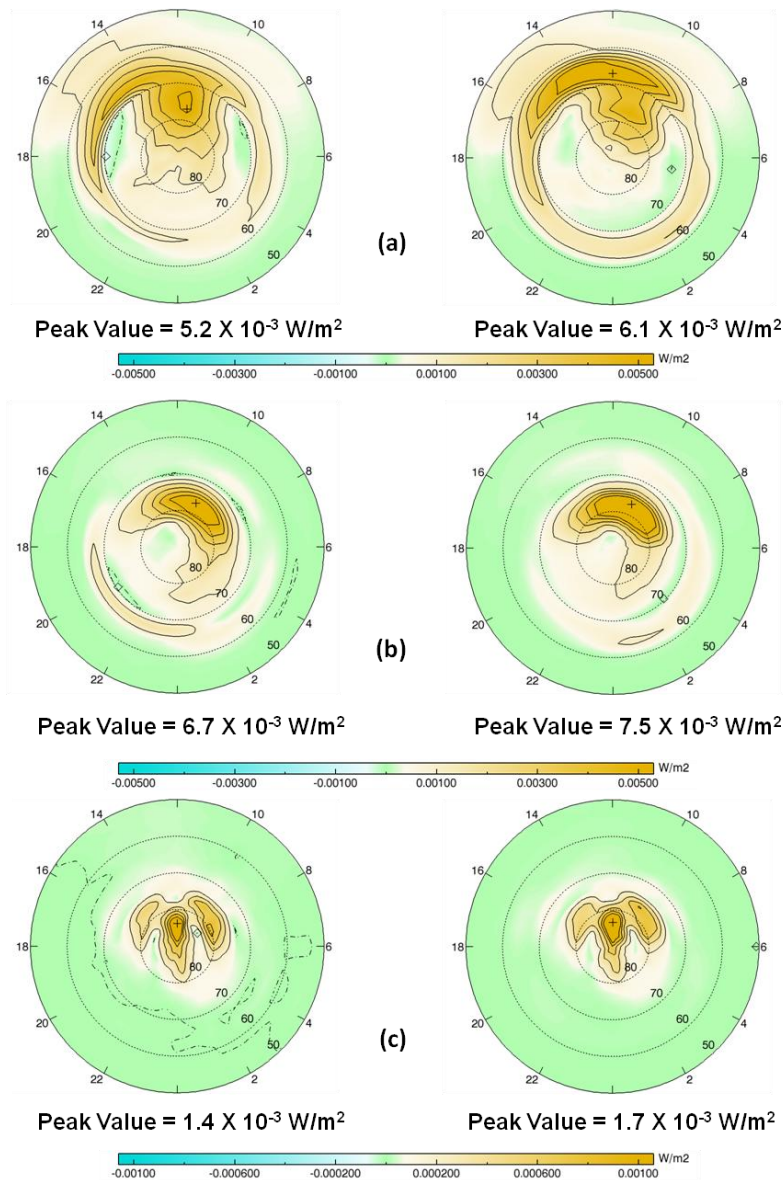


Figure 4. Poynting flux maps (left) and height-integrated power maps (right) in northern polar region for (a) South IMF; (b) East IMF; (c) North IMF. On each map the “+” symbol locates peak value.

Figure 4 shows that for the IMF East and IMF North cases, Poynting flux maps are in reasonable agreement with maps of height-integrated Joule heating. Peak values are in approximately the same location (indicated by the “+” symbol overlaid on the plots) and agree to better than 20 per cent. For the IMF South case the maps are in poorer agreement. There, Poynting flux is peaked in the convection throat region, while the integrated Joule dissipation rate is peaked in the auroral region. These results are consistent with one of the main conclusions of Richmond (2010). He found that the Poynting flux underestimates electromagnetic energy dissipation in regions of high ionospheric Pedersen conductance, and overestimates dissipation in regions of low conductance. The top two plots of Figure 4 confirm this with the Poynting flux being less than the dissipation rate in the auroral ring (region of high conductance) and greater than the dissipation rate in the convection throat (region of low conductance).

4.2. Effect of Drag-Driven Neutral Winds on Thermospheric Density

In this section we investigate how mechanical work done by the $\vec{J} \times \vec{B}$ force (or equivalently the ion drag force) on the neutrals alters thermospheric density profiles. Ultimately this is an investigation into how that force, together with other thermospheric forces such as pressure gradient, centrifugal, and Coriolis forces, determines particular steady-state horizontal density structures at different altitudes. Here we focus on two altitudes that capture two distinct ion velocity patterns: 400 km and 120 km. Figure 2 illustrates these patterns for the IMF South, East, and North cases. At the higher altitude the flow patterns are largely rotational. IMF South exhibits two circulation cells of approximately equal magnitude (the tilt of the pattern is due to the Hall conductance). IMF East also has two circulation cells, but the poleward cell is considerably larger than the equatorward cell. IMF North has four circulation cells with the largest pair having a sunward convection region at its center. These are the canonical patterns for their respective IMF orientation (e.g. Weimer, 2004). In contrast, at the lower altitude where the Hall conductivity dominates, the patterns are largely irrotational. Note the regions of convergence and divergence of the velocity vectors in these patterns. We can expect that the compressibility properties of these patterns will be imposed on the neutral fluid through the ion drag force.

Neutral Flows and Density at 400 km

Figure 3 shows the neutral velocity flow pattern and horizontal density profile of the thermosphere at 400 km altitude for the IMF East, South, and North cases. Two sets of plots are shown for the IMF East case because of the anti-symmetry of the northern and southern polar regions for this case. In all cases the neutral flow vectors track pretty closely the corresponding ion velocity vectors (see left column of plots of Figure 2). Because the neutrals are not constrained by the magnetic field, the momentum imparted to them by the ions at high latitudes enables them to slip through the ions at lower latitudes. This is particularly evident in the IMF East case where the low-latitude, nightside vectors are directed toward lower latitudes rather than turning sunward as they do in the corresponding ion vector plot.

The color coding on the neutral density plots of Figure 3 is such that blue indicates a density low, and orange-red indicates a density high. In all cases a low density cell is centered on the strongest circulation centers. For the IMF East case there is only one low density cell in each hemisphere. For the IMF North and South cases there are two low density cells. According to geostrophic adjustment theory, density and pressure lows are associated with cyclonic winds (counterclockwise in the northern hemisphere when viewed from above), and density and pressure highs are associated with anti-cyclonic winds (clockwise in the northern hemisphere when viewed from above). The plots in Figure 3 indicate that

Partitioning of Electromagnetic Energy Inputs to the Thermosphere
Final Report for FA9550-09-C-0207

only the dawn-side low for IMF South and the dusk-side low for IMF North are consistent with geostrophic force balance. The flows around the low-density cells for IMF East, the dusk-side low for IMF South, and the dawn-side low for IMF North are anti-cyclonic. Schoendorf et al. (1996) identify these cells as “antibaric” lows. They arise when the drag-driven circulation is strong enough to make centrifugal forces non-negligible and capable of producing a low-density cell where a high-density would otherwise appear. The results from our simulation at 400 km are consistent with their finding.

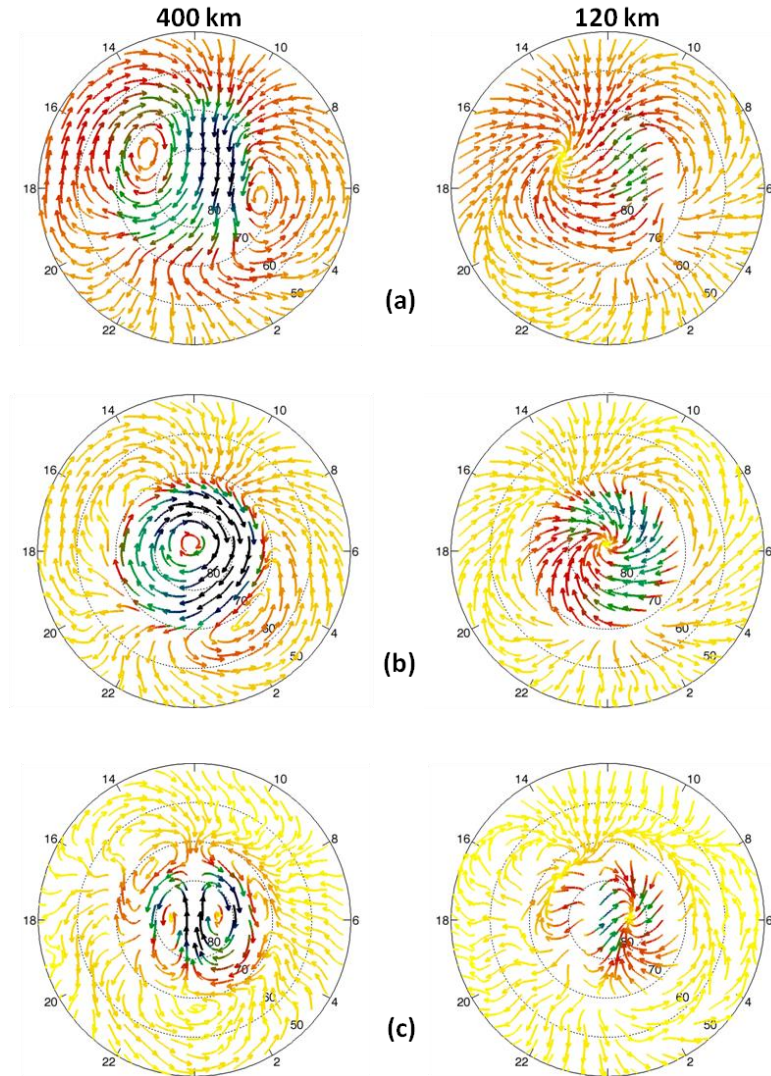


Figure 5. Ion velocity vectors at 400 km (left) and 120 km (right) for (a) IMF South; (b) IMF East; (c) IMF North. Vectors are color-coded according to magnitude with black indicating speeds equal or greater than 1 km/s for (a) and (b), and 0.5 km/s for (c).

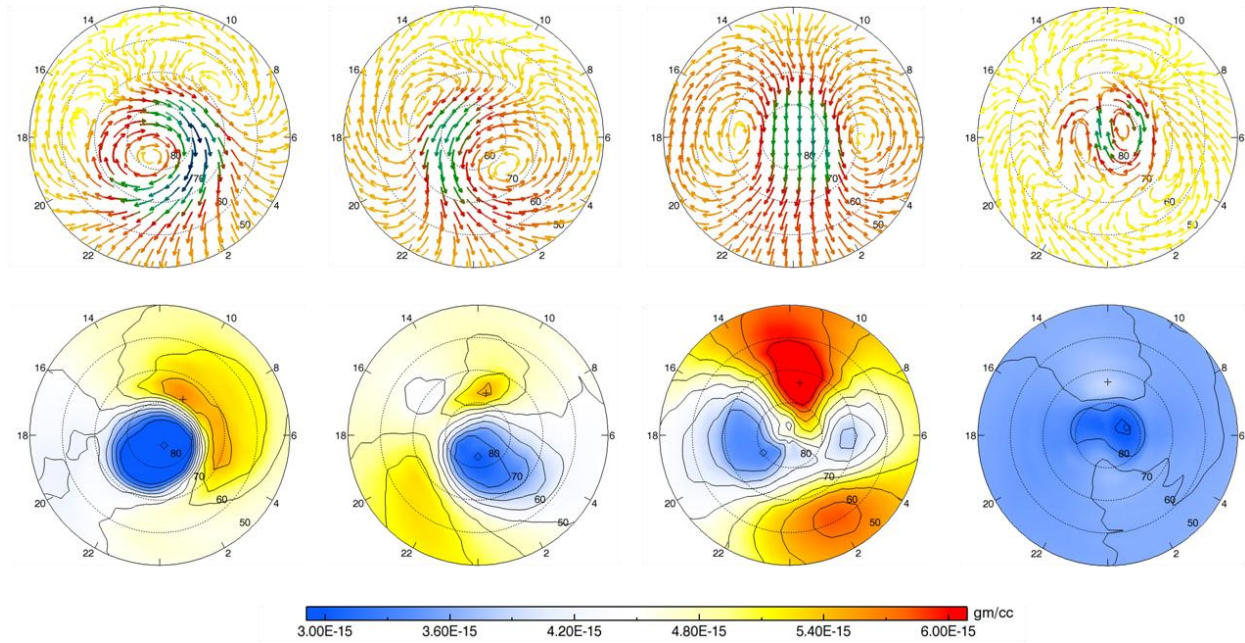


Figure 6. Neutral velocity vectors in the rotational frame (top) and neutral density contours (bottom) at 400 km. From left to right: IMF East – northern hemisphere; IMF East – southern hemisphere; IMF South; IMF North. Vectors are color-coded according to magnitude with black indicating speeds equal or greater than 1 km/s.

Further qualitative validation of the cell structure shown in the density plots of Figure 3 can be obtained by comparing them with density maps derived from CHAMP data by Kwak et al. (2009). Figure 4 reproduces a plot from their paper. The maps in Figure 4 (Figure 6 in Kwak et al) were generated by subtracting the mass density map for zero IMF from mass density maps for each of the four different IMF orientations denoted in the figure. By doing this Kwak et al. are able to isolate the effects of IMF orientation. Because they are difference maps they are not directly comparable to the plots in Figure 3; however, we can still compare relative features like the locations of density highs and lows. Note that the Kwak maps were generated over the southern hemisphere and include a case with negative IMF B_y . While we did not run a negative IMF B_y case (the IMF East case had positive IMF B_y) we can use the symmetry property that for an IMF with only a B_y component, the northern hemisphere ion convection pattern for positive IMF B_y is the same as the southern hemisphere pattern for negative IMF B_y . Therefore we expect the leftmost plot of the Kwak figure (IMF B_y negative / southern hemisphere) to correspond to the leftmost plot of Figure 3 (IMF B_y positive / northern hemisphere) and the second to left plot of the Kwak figure (IMF B_y positive / southern hemisphere) to correspond to the second to left plot of Figure 3 (also IMF B_y positive / southern hemisphere). While there are differences, many of the features seen in the data are reproduced in the ISM simulations. For negative B_y (positive B_y in the northern hemisphere) both data and simulation exhibit enhanced density on the dawn-side, and reduced density on the dusk-side (leftmost plots in Figures 3 and 4). This pattern is reversed for positive B_y (second plot from the left in Figures 3 and 4). For negative B_z both data and simulation have a large density peak in the cusp region (third plot from the left in Figures 3 and 4). This is co-located with the throat of the convection pattern. The data indicate that the dusk-side low is deeper than the dawn-side low, while the ISM simulations have the opposite polarity. It is difficult to compare the case for positive IMF B_y , since the effects are much weaker for that case (rightmost plots in Figures 3 and 4).

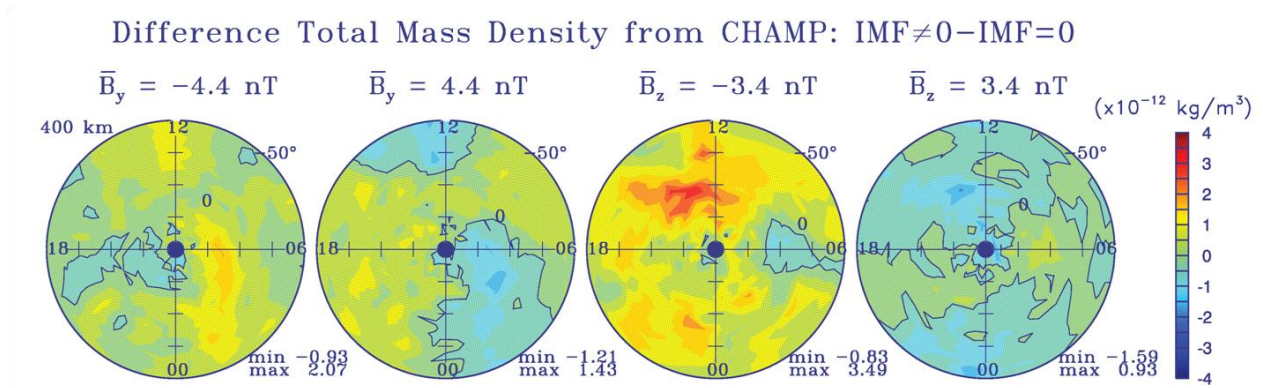


Figure 7. Figure 6 from Kwak et al. (2009). Difference densities at 400 km altitude over the southern hemisphere for different IMF orientations.

Neutral Flows and Density at 120 km

Figure 5 shows neutral velocity vectors at 120 km altitude for the IMF East, South, and North cases. As in the discussion above, we use the southern hemisphere plot for the IMF East case to represent the northern hemisphere result from a negative IMF B_y simulation. As we observed at 400 km altitude, the neutral velocity pattern is characterized by a two-cell convection pattern for the IMF East and South cases. For these cases the two-cell pattern is rotated by approximately 4 – 6 hours to the east (counterclockwise in the plots) with respect to the higher-altitude ion convection pattern (see the left column of Figure 2). This rotation of the convection pattern is consistent with predictions from the analytic model of Mikkelsen and Larsen (1983). It is a consequence of the Coriolis force. We have observed in other simulations (not reported on here) that when co-rotation is artificially turned off, the velocity pattern aligns with the ion pattern.

For the IMF North case the flow pattern is more complex, with multiple circulation cells. Closer inspection of the neutral velocity pattern for this case indicates that it too is a rotated version of the high-altitude ion convection pattern. This is especially evident upon examination of a series of velocity vector plots that begin at 400 km altitude and end at 120 km altitude, because the degree of rotation is gradual and increases with decreasing altitude. Using this technique we determined that the 120 km pattern for the IMF case is rotated approximately 10 hours to the east with respect to the high-altitude ion convection pattern. There is also deformation of the circulation cells which is why it is difficult to ascertain the degree of rotation in the plot of Figure 5. It is likely that the greater degree of rotation is a consequence of the weaker ion driver for this case.

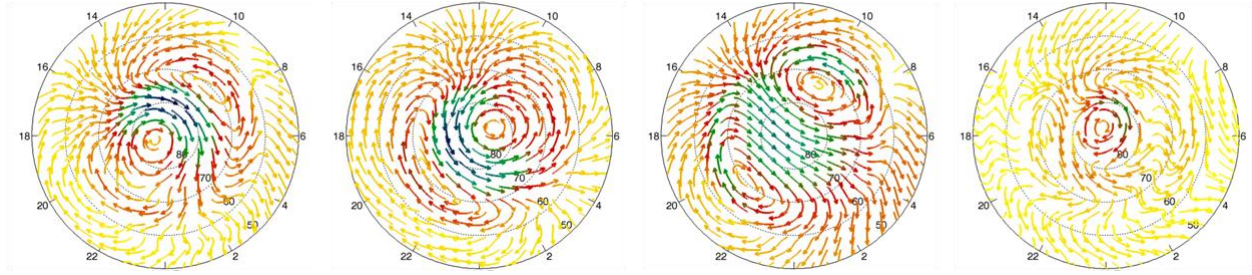


Figure 8. Neutral velocity vectors in the rotational frame at 120 km. From left to right: IMF East – northern hemisphere; IMF East – southern hemisphere; IMF South; IMF North. Vectors are color-coded according to magnitude with black indicating speeds equal or greater than 0.1 km/s.

Next we examine the neutral density cell structure at 120 km altitude. Figure 6 contains neutral density contour plots together with vector plots of the $\vec{J} \times \vec{B}$ force. Before discussing the rationale for comparing $\vec{J} \times \vec{B}$ vectors with neutral density contours, we will first compare the neutral density cell structure to the neutral velocity vectors of Figure 5. For the positive IMF B_y case (leftmost plot) we see that the density high corresponds to the center of an anti-cyclonic circulation region, and the density low centered at morning corresponds to the center of a cyclonic circulation region. Thus these results are consistent with geostrophic theory. (Note that the range of the density scale at this altitude is much smaller than for the corresponding plots at 400 km).

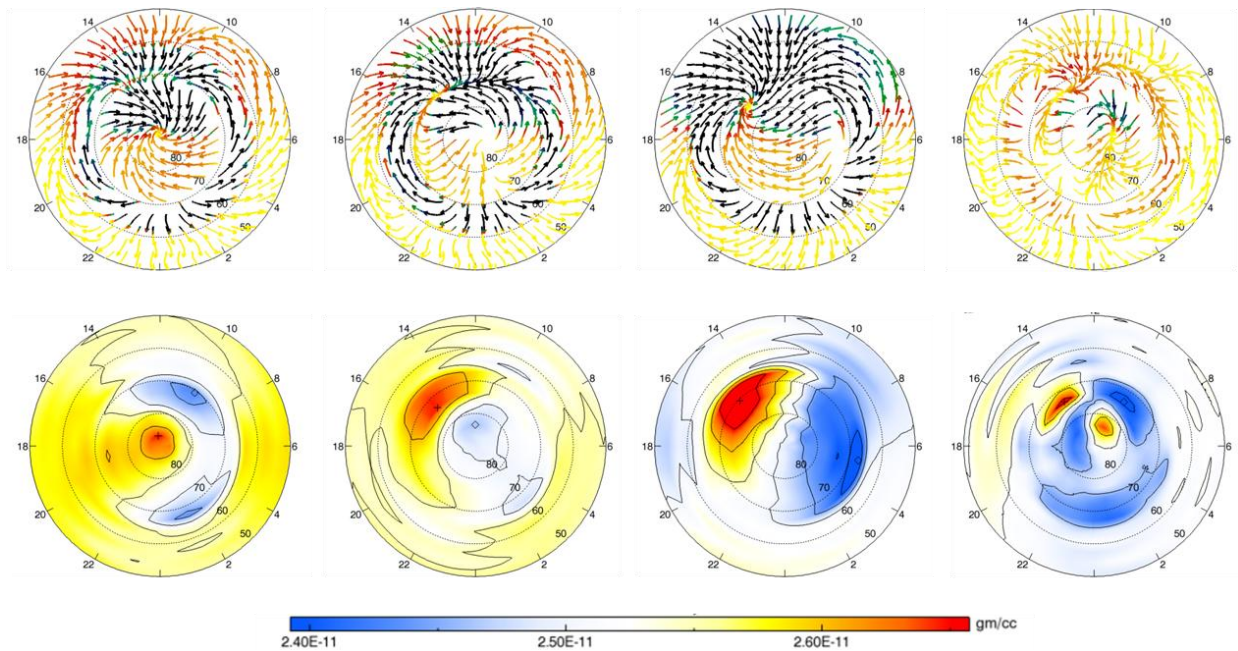


Figure 9. $\vec{J} \times \vec{B}$ vectors (top) and neutral density contours (bottom) at 120 km. From left to right: IMF East – northern hemisphere; IMF East – southern hemisphere; IMF South; IMF North. Vectors are color-coded according to magnitude with black indicating $\vec{J} \times \vec{B}$ force magnitudes equal or greater than 1×10^{-11} dyne/cm³.

For the surrogate negative IMF B_y case (second plot from the left), the density low over the pole corresponds to a cyclonic circulation region, but the high is not co-located with the anti-cyclonic circulation region. For the IMF South case (third plot from the left) the density lows and highs are completely out of phase with their geostrophic circulation centers. And for the IMF North case it is difficult to correlate any of the four distinct density cells over the pole with a geostrophic circulation center.

Because of these inconsistencies we looked to an alternative explanation for the 120 km neutral density cell structure. Although the neutral flow patterns at 120 km altitude appear to be largely rotational convection patterns, as we alluded to in Section 4.2, the ion velocity pattern at 120 km altitude (see right column of plots in Figure 2) is largely irrotational with regions of convergent and divergent vector directions. This velocity pattern gets impressed upon the neutrals through the ion drag force. As shown in Section 2.1 the ion-neutral drag force is proportional to ion mass density, ion-neutral collision frequency, and the vector velocity difference between ion and neutral velocities. In steady state it is balanced by the $\vec{J} \times \vec{B}$ force. Thus we look to vector plots of $\vec{J} \times \vec{B}$ to identify regions where the ion drag force is acting to create neutral flow divergences, and thus density enhancements and depressions.

For all of the cases shown in Figure 6 we see that the regions of convergence correspond to density enhancements and regions of divergence correspond to density depressions. Thus the neutral density cell structure in regions where the Hall conductivity dominates is organized by the $\vec{J} \times \vec{B}$ force and concomitantly by the rotation of the ion velocity pattern from a predominantly rotational pattern at high altitudes to a predominantly irrotational pattern at low altitudes. This is one of the major conclusions of this research effort. It suggests that if we know the morphology of the high-altitude velocity pattern, and have a reasonable representation of the Hall conductivity, we can predict where the high and low density cells will appear. As described in Liu et al. (2004) the prediction of pressure/density cells in the thermosphere and their attendant causes could be provide a useful framework to order and interpret high-latitude neutral density data.

4.3. Feedback Mechanisms

There are a variety of mechanisms by which neutral dynamics can feed back and alter the Poynting flux that transmits electromagnetic energy from the magnetosphere to the ionosphere / thermosphere. In this section we consider the effects of the drag-driven neutral winds. As momentum is transferred to the thermosphere by ion-drag, neutral winds increase and the velocity difference between ions and neutrals decreases. The rate at which this occurs depends on collision frequency and neutral mass density. As the velocity difference decreases, less current is required from the magnetospheric dynamo (recall from Section 2.1 that in steady state the drag force is balanced by the $\vec{J} \times \vec{B}$ force). If the dynamo is a constant voltage generator, the system responds as it would to a decrease in conductivity, and Poynting flux would be reduced. If, on the other hand, the dynamo acts more like a constant current source, the system would respond to maintain the velocity difference between ions and neutrals and further accelerate both fluids, perhaps resulting in an increase of Poynting flux into the thermosphere.

To examine these potential effects we can take advantage of the artifice we employed to perform our coupled simulations. For each simulation we attained a magnetospheric steady state by first using a static neutral atmosphere, i.e. the neutral velocity was set to zero. The thermospheric simulation phase was then performed by driving the thermosphere for 24 hours with these fixed magnetosphere conditions, allowing the neutral winds to ramp up to equilibrium values. Thus by comparing

electrodynamic quantities when neutral velocities are zero (large ion-neutral velocity difference) with those after neutral velocities have ramped up (smaller ion-neutral velocity difference) we can assess the feedback path discussed above.

Figure 10 contains plots of electrodynamic quantities for zero neutral velocity (left column) and steady-state neutral velocity (right column) for the IMF South case. The top pair of plots contains $\vec{J} \times \vec{B}$ vectors at 300 km, near the F-region conductivity peak. At zero neutral velocity the pattern looks exactly like the ion velocity pattern (see the top left plot of Figure 5). This is a consequence of the force balance equation of Section 2.1 when neutral velocity is set to zero. For steady-state neutral winds, the magnitude of the $\vec{J} \times \vec{B}$ force is greatly reduced, in agreement with the arguments presented above. The bottom pair of plots contains the $\vec{J} \times \vec{B}$ vectors at 120 km altitude, near the E-region conductivity peak. Here the plots for the two cases are indistinguishable. This is a consequence of the fact that even after 24 hours of steady ion-driving, the magnitude of the neutral winds is still a small fraction of the ion velocity because of the much larger neutral mass density at this altitude. The middle set of plots shows the global effect of the neutral dynamics in terms of the parallel currents that couple the magnetosphere with the ionosphere/ thermosphere. These currents are plotted on an altitude surface at 500 km. Their close similarity indicates that despite the fact that the F-region is drawing less current, the magnitude of this current decrement is so small that it does not alter the global electrodynamics of the coupled system. These are controlled at E-region altitudes where the large neutral mass densities inhibit neutral flows that would otherwise alter current closure properties.

5. Conclusions

We have used a numerical model of the coupled solar wind – magnetosphere – ionosphere – thermosphere to elucidate some of the fundamental processes that govern thermospheric response to electromagnetic energy inputs. We studied three main subject areas: energy partitioning, horizontal neutral density structures, and feedback of neutral dynamics to the coupled system.

In the area of electromagnetic energy partitioning, we determined that for all of the IMF orientations we studied, approximately 90 per cent of the electromagnetic energy goes into Joule heating for steady-state conditions. So in a global sense, measurements of Joule heating rates provide a good approximation to total electromagnetic energy input; however, locally this is not always the case. For example, under southward IMF orientations, local height-integrated Joule heating rates overestimate Poynting flux in regions of high conductance, and underestimate Poynting flux in regions of lower conductance. This confirms a prediction of Richmond (2010).

In the area of neutral density structures at F-region altitudes, we confirmed the analysis of Schoendorf et al (1996) that attributed the existence of anti-cyclonic low density cells to centrifugal effects in the presence of large drag-driven neutral flows. At E-region altitudes, we presented a new theory that relates neutral density cell structure to divergences of the $\vec{J} \times \vec{B}$ force. At E-region altitudes these divergences arise because of Hall conductivity effects which rotate current-density and ion-velocity vectors from their non-divergent F-region patterns.

In the area of feedback effects, we found that increases in neutral wind speeds under steady driving conditions do not significantly alter electromagnetic energy flows into the ionosphere / thermosphere. While F-region closure currents were significantly reduced, the much larger E-region closure currents were not, owing to the much larger neutral densities, and thus much greater coupling times.

Partitioning of Electromagnetic Energy Inputs to the Thermosphere
Final Report for FA9550-09-C-0207

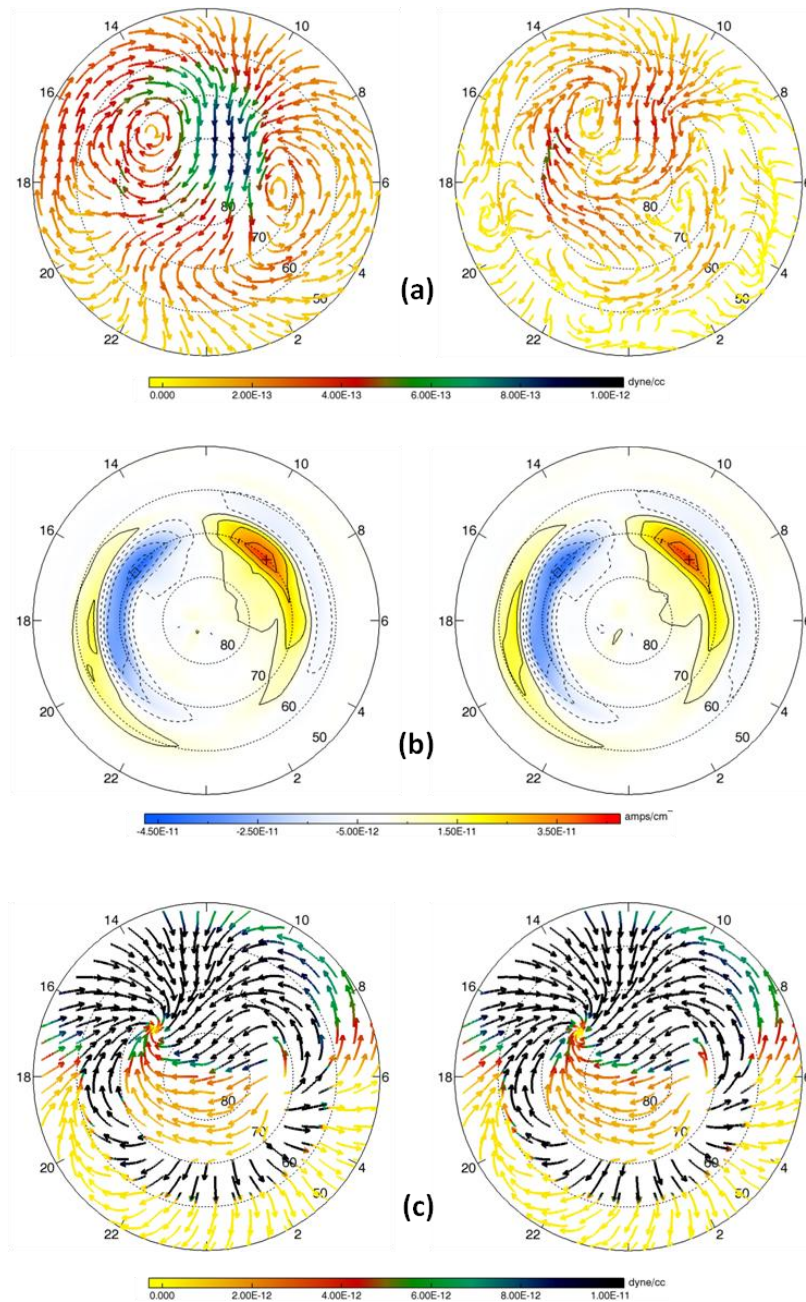


Figure 10. Electrodynamics for simulations with zero neutral velocity (left column) and steady-state neutral velocity (right column). (a) $J \times B$ vectors at 300 km altitude; (b) Parallel current density contours at 500 km altitude (orange-red indicates current into ionosphere; blue indicates current out of the ionosphere); (c) $J \times B$ vectors at 120 km altitude

6. Personnel Supported

Keith Siebert (PI – ARA)

Jackie Schoendorf (Co-PI – ARA)

George Siscoe (Boston University – Consultant)

7. Publications

George Siscoe submitted a paper entitled “Aspects of Global Coherence of Magnetospheric Behavior” to Journal of Atmospheric and Terrestrial Physics. This paper contains insights gleaned from ISM simulations performed for this contract. Contract acknowledgment was included.

George Siscoe presented a poster at the 2011 GEM/CEDAR meeting titled “Possible explanation of the Love-Gannon relationship between Dst and the local-time asymmetry in the low-latitude disturbance field”. The work he presented was partially funded by this project.

8. Interactions / Transitions

Early in this reporting period we consulted with William Burke and Dan Ober of AFRL (Hanscom AFB). They provided program direction for the initial phases of this project.

Keith Siebert gave a presentation at the AFOSR Space Sciences Program Review held in Albuquerque, NM on 23 June 2011. The title of his presentation was “Electromagnetic Energy Partitioning in the Polar Thermosphere”.

Keith Siebert and Jackie Schoendorf met with Dolores Knipp (High Altitude Observatory, NCAR) at the ARA Nashua office in July 2011. They discussed Dolores’ research interest in intense Poynting flux enhancement during IMF B_y events (Knipp, 2011). We incorporated her suggestions into our simulation analysis.

Keith Siebert gave an invited presentation at the University of Massachusetts – Lowell Center for Atmospheric Research (UMLCAR) on the research described in this report. The title of the presentation was “Studies of Electromagnetic Energy Partitioning in the Polar Thermosphere with the Integrated Space Weather Prediction Model (ISM)”. Interactions with UMLCAR staff provided ideas to achieve research objectives for this project.

9. References

Deng, Y., T. J. Fuller - Rowell, R. A. Akmaev, and A. J. Ridley (2011), Impact of the altitudinal Joule heating distribution on the thermosphere, *J. Geophys. Res.*, 116, A05313, doi:10.1029/2010JA016019.

Kwak, Y.-S., A. D. Richmond, Y. Deng, J. M. Forbes, and K.-H. Kim (2009), Dependence of the high-latitude thermospheric densities on the interplanetary magnetic field, *J. Geophys. Res.*, 114, A05304, doi:10.1029/2008JA013882.

Li, W., D. Knipp, J. Lei, and J. Raeder (2011), The relation between dayside local Poynting flux enhancement and cusp reconnection, *J. Geophys. Res.*, 116, A08301, doi:10.1029/2011JA016566.

Liu, H., H. Lühr, V. Henize, and W. Köhler (2005), Global distribution of the thermospheric total mass density derived from CHAMP, *J. Geophys. Res.*, 110, A04301, doi:10.1029/2004JA010741.

Richmond, A. D. (2010), On the ionospheric application of Poynting’ s theorem, *J. Geophys. Res.*, 115, A10311, doi:10.1029/2010JA015768.

Schoendorf, J. G., G. Crowley, R. G. Roble, and F. A. Marcos (1996), Neutral density cells in the high latitude thermosphere—1. Solar maximum cell morphology and data analysis, *J. Atmos. Terr. Phys.*, 58, 1751– 1768.

Partitioning of Electromagnetic Energy Inputs to the Thermosphere
Final Report for FA9550-09-C-0207

White, W. W., J. A. Schoendorf, K. D. Siebert, N. C. Maynard, D. R. Weimer, G. L. Wilson, B. U. Ö. Sonnerup, G. L. Siscoe, and G. M. Erickson (2001), MHD simulation of magnetospheric transport at the mesoscale, *Space Weather, Geophysical Monograph Series Vol. 125*, edited by Paul Song, Howard J. Singer, and George L. Siscoe, pp. 229-240, American Geophys. Union.

Weimer, D. R. (2005), Improved ionospheric electrodynamic models and application to calculating Joule heating rates, *J. Geophys. Res.*, 110, A05306, doi:10.1029/2004JA010884.

Vasyliūnas, V. M., and P. Song (2005), Meaning of ionospheric Joule heating, *J. Geophys. Res.*, 110, A02301, doi:10.1029/2004JA010615.